



## Article

# The Influence of Titanium Dioxide on Silicate-Based Glasses: An Evaluation of the Mechanical and Radiation Shielding Properties

Badriah Albarzan <sup>1</sup>, Mohamed Y. Hanfi <sup>2,3</sup> , Aljawhara H. Almuqrin <sup>1</sup>, M. I. Sayyed <sup>4,5,\*</sup> , Haneen M. Alsafi <sup>6</sup> and K. A. Mahmoud <sup>7,8,\*</sup> 

- <sup>1</sup> Department of Physics, College of Science, Princess Nourah bint Abdulrahman University, Riyadh 11671, Saudi Arabia; baalbarzan@pnu.edu.sa (B.A.); ahalmoqren@penu.edu.sa (A.H.A.)
- <sup>2</sup> Institute of Physics and Technology, Ural Federal University, Mira St 19, 620002 Ekaterinburg, Russia; mokhamed.khanfi@urfu.ru
- <sup>3</sup> Department of Medical and Radiological Research, Research Sector, Nuclear Materials Authority, P.O. Box 530 El-Maadi, Cairo 520, Egypt
- <sup>4</sup> Department of Physics, Faculty of Science, Isra University, Amman 11622, Jordan
- <sup>5</sup> Department of Nuclear Medicine Research, Institute for Research and Medical Consultations, Imam Abdulrahman Bin Faisal University, Dammam 31441, Saudi Arabia
- <sup>6</sup> Department of Magnetism and Magnetic Nanomaterials, Natural and Mathematical Institute, Ural Federal University, St Kuibysheva 48, 620026 Yekaterinburg, Russia; haneenalsafi.1991@gmail.com
- <sup>7</sup> Department of Nuclear Power Plants and Renewable Energy Sources, Ural Power Engineering Institute, Ural Federal University, St. Mira 19, 620002 Yekaterinburg, Russia
- <sup>8</sup> Department of Analytical Chemistry, Production Sector, Nuclear Materials Authority, P.O. Box 530 El-Maadi, Cairo 520, Egypt
- \* Correspondence: mabuallssayed@ut.edu.sa (M.I.S.); kmakhmud@urfu.ru (K.A.M.)



**Citation:** Albarzan, B.; Hanfi, M.Y.; Almuqrin, A.H.; Sayyed, M.I.; Alsafi, H.M.; Mahmoud, K.A. The Influence of Titanium Dioxide on Silicate-Based Glasses: An Evaluation of the Mechanical and Radiation Shielding Properties. *Materials* **2021**, *14*, 3414. <https://doi.org/10.3390/ma14123414>

Academic Editor: Daniel Kiener

Received: 17 May 2021

Accepted: 18 June 2021

Published: 20 June 2021

**Publisher's Note:** MDPI stays neutral with regard to jurisdictional claims in published maps and institutional affiliations.



**Copyright:** © 2021 by the authors. Licensee MDPI, Basel, Switzerland. This article is an open access article distributed under the terms and conditions of the Creative Commons Attribution (CC BY) license (<https://creativecommons.org/licenses/by/4.0/>).

**Abstract:** The mechanical and radiation shielding features were reported for a quaternary Na<sub>2</sub>O-CaO-SiO<sub>2</sub>-TiO<sub>2</sub> glass system used in radiation protection. The fundamentals of the Makishima-Mazinize model were applied to evaluate the elastic moduli of the glass samples. The elastic moduli, dissociation energy, and packing density increased as TiO<sub>2</sub> increased. The glasses' dissociation energy increased from 62.82 to 65.33 kJ/cm<sup>3</sup>, while the packing factor slightly increased between 12.97 and 13.00 as the TiO<sub>2</sub> content increased. The MCNP-5 code was used to evaluate the gamma-ray shielding properties. The best linear attenuation coefficient was achieved for glass samples with a TiO<sub>2</sub> content of 9 mol%: the coefficient decreased from 5.20 to 0.14 cm<sup>-1</sup> as the photon energy increased from 0.015 to 15 MeV.

**Keywords:** silicate glass; mechanical properties; radiation shielding; MCNP5

## 1. Introduction

Attention has been drawn to radiation due to their profitable applications in nuclear medicine, agriculture, etc. [1]. However, the harm of radioactive sources limits their use. Thus, the dose rate from these radiation types should be controlled. Exposure time, source-person distance, and shielding materials are essential factors for controlling exposure [2]. The most commonly known shielding materials are glass, concrete, rock, polymers, and alloys.

The type of shielding material depends mainly on the activity of the emitted energy. The most widespread and low-cost materials for X- and gamma-ray shielding are glass, heavy bricks, painting materials, and concrete [3]. Concrete is considered one of the best materials for radiation shielding due to its reasonable cost and easy construction. Concretes containing heavy and normal aggregates have been noted as suitable shielding materials against both photons and fast neutrons due to their high hydrogenous content [4]. Despite these advantages, concrete has many drawbacks. It can be damaged by expanding

aggregates, the freezing of trapped water, infiltration, and other chemical and physical processes [5].

Glasses have some promising characteristics in terms of radiation protection, especially with regards to transparency. With vitrification, glasses containing heavy metal oxides (HMO) can reduce ionizing radiation hazards and keep radioactive waste chemically stable state for a long time [6]. Therefore, glasses provide transparent, light, and low-volume materials with better shielding properties [7].

Radiation shielding glasses using borate [8–10], phosphate, and silicate have been developed. In many applications, silicate glasses satisfy the majority of requirements [11,12]. Commercial glasses are recommended due to the ease of fabrication and the excellent provision of visibility. The absorbance and transmission of visible light are affected mainly by glass thickness and chemical composition. Increasing glass thickness will help increase the absorption edge.

Most silicate glasses are used in windows with the addition of a small amount of alkaline oxides [13]. The high atomic number of lead enhances gamma-ray attenuation. Consequently, the addition of small amounts of Na<sub>2</sub>O to lead oxide-based silicate glass facilitates the melting process and produces promising attenuation properties [14].

A detailed theoretical study on the mechanical properties of silicate-based lead oxide glass is provided in the present work. Furthermore, the efficiency of the investigated samples in attenuating gamma rays is examined using the Monte simulation.

## 2. Materials and Methods

Six NaO<sub>2</sub>-CaO-SiO<sub>2</sub>-TiO<sub>2</sub> glass samples were created. Such compounds are discussed in Limbach et al. [15]. The replacement of SiO<sub>2</sub> with TiO<sub>2</sub> significantly affects the physical characteristics (density  $\rho$ , molar volume  $V_M$ , and molecular weight  $M_W$ ) of the quaternary Na<sub>2</sub>O-CaO-SiO<sub>2</sub>-TiO<sub>2</sub> glass system. Figure 1 illustrates that density ( $\rho$ , g/cm<sup>3</sup>) increased slightly (between 2.560 and 2.661 g/cm<sup>3</sup>), while molar volume ( $V_m$ , cm<sup>3</sup>/mol) declined from 23.51 to 23.21 cm<sup>3</sup>/mol. The behavior presented in Figure 1 is attributed to the partial replacement of SiO<sub>2</sub> ( $\rho_{\text{SiO}_2} = 2.65$  g/cm<sup>3</sup> and  $MW_{\text{SiO}_2} = 60.08$  g/mol) with TiO<sub>2</sub> ( $\rho_{\text{TiO}_2} = 4.23$  g/cm<sup>3</sup> and  $MW_{\text{SiO}_2} = 79.86$  g/mol).

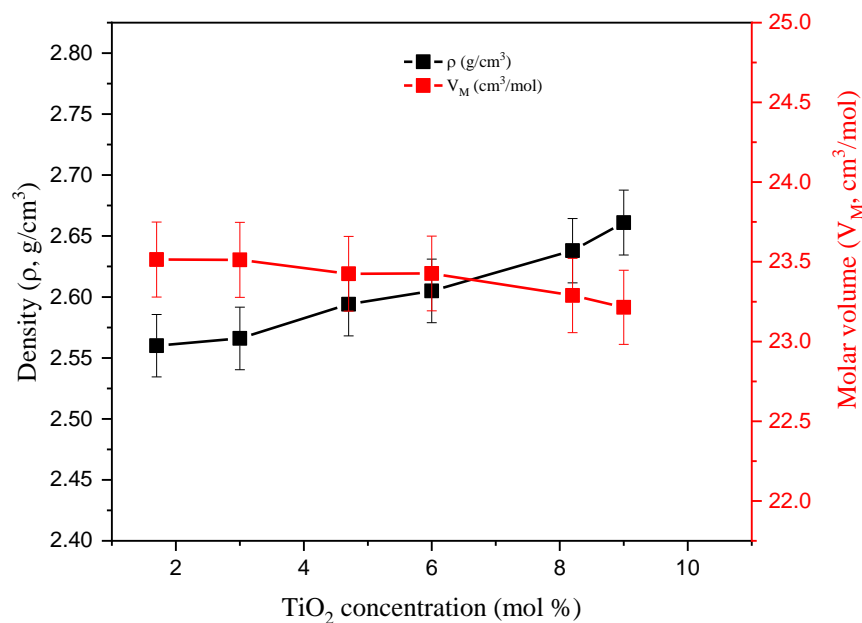


Figure 1. Variation of glass density and molar volume versus TiO<sub>2</sub> concentration.

### 2.1. Mechanical Properties

The elastic moduli (EM) and some mechanical properties were investigated. These calculations are based on the foundations provided by Makishema and Makinsize in 1973 and 1975 [16,17]. They assumed that glass atoms are found separately in the matrix and that the bonds between atoms are affected by the dissociation energy ( $G_i$ ) of the constituting compounds, as well as the ionic radii of metals ( $R_M$ ) and oxides ( $R_O$ ). The total dissociation energy ( $G_t$ ) of the investigated glass samples describes the amount of heat required to bind the metal-oxygen atoms:  $G_t$  (kJ/cm<sup>3</sup>) =  $\sum X_i G_i$ , where  $X_i$  refers to the molar fraction of the investigated samples. The packing density ( $V_t$ ) is related to the previously mentioned ionic radii  $R_O$  and  $R_M$ , where  $V_t = (\rho/MW) \times \sum X_i V_i$ ;  $V_i$  is the packing factor of the constituting compounds,  $\rho$  is the glass density, and MW is the molar weight of the glass.

Starting from  $G_t$  and  $V_t$ , the EM moduli (Young ( $E$ ), bulk ( $B$ ), shear ( $K$ ), longitudinal ( $L$ )), and some mechanical properties are predicted. These mechanical properties are the Poisson ratio ( $\zeta$ ), micro-hardness ( $H$ ), the softening temperature ( $T_s$ ), and fractal bond connectivity ( $d$ ) [18]:

$$E \text{ (GPa)} = 2V_t G \quad (1)$$

$$B \text{ (GPa)} = 1.2 V_t E \quad (2)$$

$$S \text{ (GPa)} = \frac{3EB}{(9B - E)} \quad (3)$$

$$L \text{ (GPa)} = B + \frac{3}{4} S \quad (4)$$

$$\sigma = 0.5 - \frac{1}{7.2} V_t \quad (5)$$

$$H \text{ (GPa)} = \frac{(1 - 2\sigma)}{6(1 + \sigma)} \quad (6)$$

$$T_s \text{ (C)} = \frac{M_W}{(\rho_{glass} \times C)} \times V_s^2 \quad (7)$$

### 2.2. Shielding Properties

The gamma-ray shielding features were simulated using the Monte Carlo simulation method [19] and Phy-X/PSD software [20]. Both methods use chemical compositions and densities to evaluate shielding factors. However, they use distinct nuclear libraries, which are the most important files for extracting interaction cross-sections. MCNP-5 uses ENDF/B-VI.8 as a primary source, while the Phy-X/PSD program uses the NIST database (like XCOM software).

MCNP-5 needs an input file containing geometry, cells, surfaces, sources, and detectors. Figure 2 is a 3D representation of the current input file. It shows a Pb cylinder (thickness = 5 cm, height = 35 cm, and diameter = 30 cm) and filled with dry air. This cylinder is used to isolate the equipment from external background radiation.

Inside the lead cylinder, some tools were arranged to make the simulation geometry similar to the narrow beam transmission experiment, where a source was placed in the geometry center. A lead collimator followed the source, which is then followed by the glass samples, another lead collimator, and the detector (F4 tally). The F4 tally was chosen to predict the gamma-ray average track length (ATL) over the detector cell. The dimensions of the components are illustrated in Figure 1, while the chemical composition, density, and molar volume are listed in Table 1.

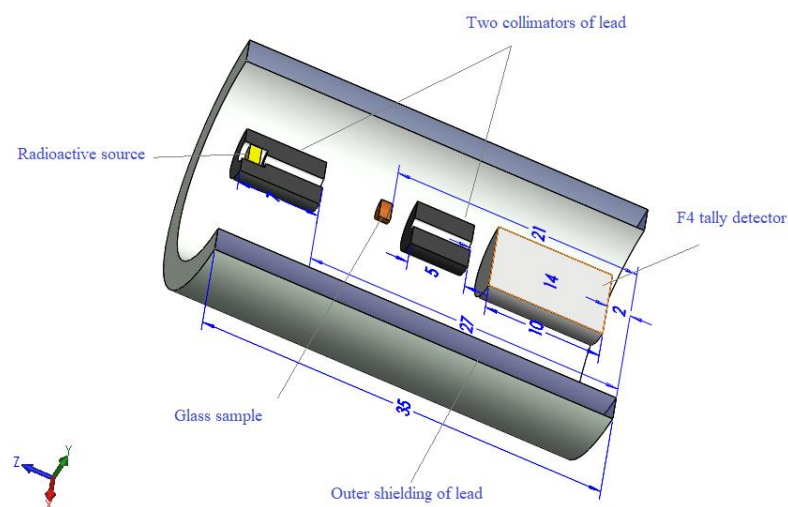


Figure 2. The 3D geometry described by the MCNP-5 input file.

Table 1. Chemical composition of the glass samples.

Samples	Chemical Composition (mol%)				Density (g/cm <sup>3</sup> )	MW (g/mol)	V <sub>m</sub> (cm <sup>3</sup> /mol)
	Na <sub>2</sub> O	CaO	SiO <sub>2</sub>	TiO <sub>2</sub>			
S1	14.6	14.0	69.8	1.7	2.6	60.2	23.5
S2	14.6	14.0	68.3	3.0	2.6	60.3	23.5
S3	15.0	13.3	67.0	4.7	2.6	60.8	23.4
S4	15.0	13.2	65.8	6.0	2.6	61.0	23.4
S5	15.1	13.9	62.8	8.3	2.6	61.4	23.3
S6	15.0	13.8	61.3	9.0	2.7	61.8	23.2

The NPS card was chosen to cut off photon interactions after running at 10<sup>8</sup> historical. A detailed explanation of the geometry used is presented in our previous publications [21,22].

The simulated ATL was fitted with the linear attenuation coefficient (LAC) as presented in Equations (8)–(10):

$$\mu_m \left( \frac{\text{cm}^2}{\text{g}} \right) = \frac{LAC \text{ (cm}^{-1}\text{)}}{\rho} \quad (8)$$

$$HVL \text{ (cm)} = \frac{\ln(2)}{LAC} \quad (9)$$

$$MFP \text{ (cm)} = \frac{1}{LAC} \quad (10)$$

### 3. Results and Discussion

#### 3.1. Mechanical Properties

Besides the enthalpy (heat of formation) of the compound and the ionic radii values, the previously stated physical parameters were applied to calculate elastic moduli (EM) based on the assumptions of the M-M model [16,17]. The  $G_t$  and  $V_t$  of the glasses are calculated (Figure 3). Both  $G_t$  and  $V_t$  increased as SiO<sub>2</sub> was replaced with TiO<sub>2</sub>.  $G_t$  is a measure of the heat of formation required to bind the glass atoms. This increased from 62.82 to 65.33 kJ/cm<sup>3</sup> as the TiO<sub>2</sub> concentration increased to 1.7 and 9 mol%, respectively. This is attributed to the higher bond dissociation energy of TiO<sub>2</sub> ( $G_i = 101.2$  kJ/cm<sup>3</sup>) compared to SiO<sub>2</sub> ( $G_i = 68$  kJ/cm<sup>3</sup>) [23]. Moreover,  $V_t$  depends mainly on the ionic radii of the

constituting compounds. The  $V_t$  values increased slightly from 0.55 to 0.56 due to the replacement of Si atoms with an ionic radius of  $R_{Si} = 8.58 \text{ \AA}$  with Ti atoms ( $R_{Ti} = 14 \text{ \AA}$ ).

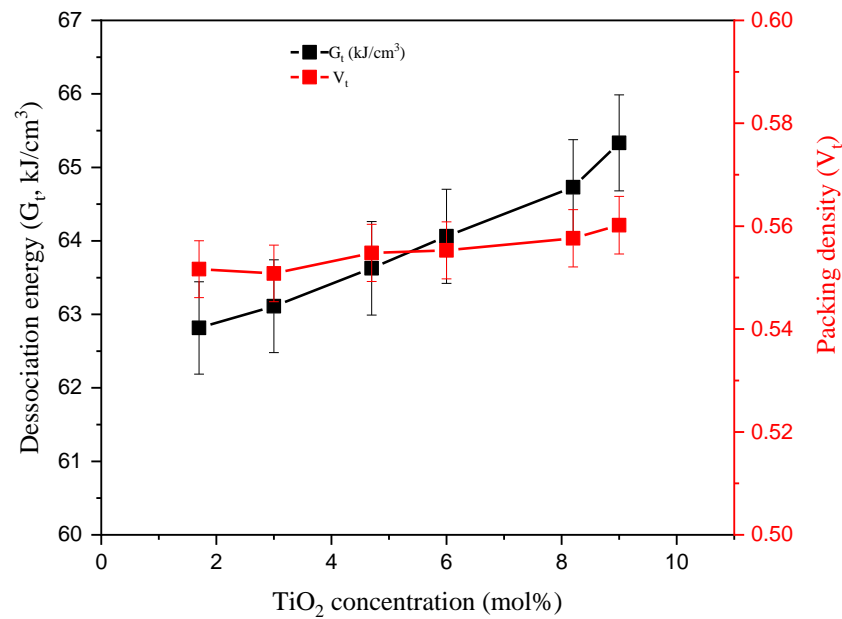


**Figure 3.** Variation of the dissociation energy ( $G_t$ ) and the packing density ( $V_t$ ) versus TiO<sub>2</sub> concentration.

EM like the Young ( $E$ ), bulk ( $B$ ), shear ( $K$ ), and longitudinal ( $L$ ) properties were also calculated based on the predicted values of  $G_t$  and  $V_t$ . Figure 4 illustrates that  $E$ ,  $B$ ,  $S$ , and  $L$  increased as TiO<sub>2</sub> content increased.  $E$  increased from 69.30 to 73.20 GPa as the substitution of Si<sub>2</sub>O with Ti<sub>2</sub>O increased from 1.7 to 9 mol%, respectively. The other moduli followed the trend of  $E$ . The  $B$ ,  $K$ , and  $L$  moduli changed between 45.88–49.21 GPa, 27.76–29.23 GPa, and 82.89–88.18 GPa, respectively. The increase of  $E$  is due to the increase in  $V_t$  as a result of the substitution of Si-O bonds with Ti-O bonds. The calculations of  $B$ ,  $K$ , and  $L$  are based on the  $E$  modulus (Equations (1)–(4)). Thus, they follow the same trend.

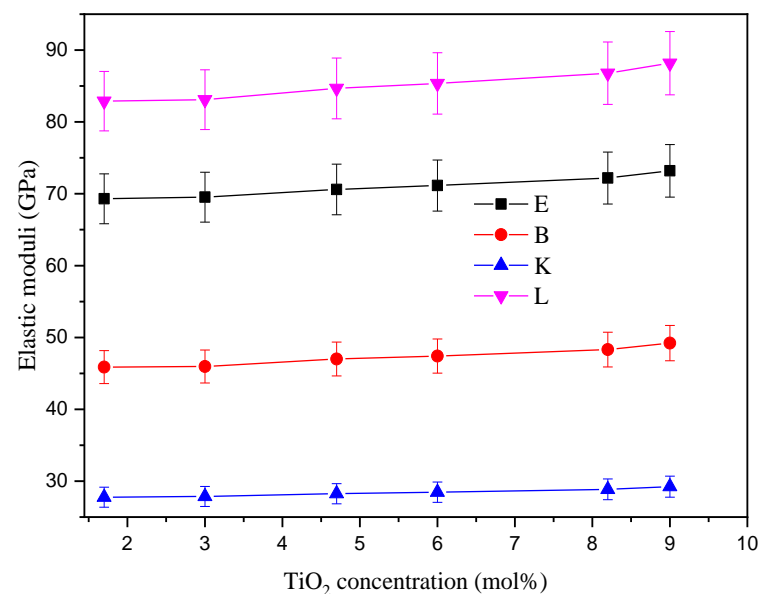


**Figure 4.** Variation of elastic moduli like the Young ( $E$ ), bulk ( $B$ ), shear ( $K$ ), and longitudinal ( $L$ ) properties as a function of TiO<sub>2</sub> concentration.

Hardness is considered one of the most important mechanical properties for shielding materials. In the current study, microhardness ( $H$ , GPa) was introduced to define the hardness of these micro-scale materials. In the microhardness tests, the loads were lighter than 1 kg (less than 10 Newtons). Figure 5 shows the change in the microhardness of the glass samples when the  $\text{TiO}_2$  concentration increases from 1.7 to 9 mol%. The  $H$  values increased gradually with the  $\text{TiO}_2$  concentration, which is related to the replacement of Si-O bonds with relatively strong bonds (i.e., Ti-O).  $H$  has values of 4.66, 4.68, 4.71, 4.75, 4.79, and 4.83 GPa for glass samples with  $\text{TiO}_2$  content of 1.7, 3, 4.7, 6, 8.2, and 9 mol%, respectively. The Poisson ratio ( $\zeta$ ) is also a measure for expanding the investigated glasses perpendicular to the compression direction. This is illustrated in Figure 5, where it follows the behavior of  $H$ . The  $\zeta$  values increase from 0.248 to 0.252 with the partial replacement of  $\text{SiO}_2$  with  $\text{TiO}_2$ .

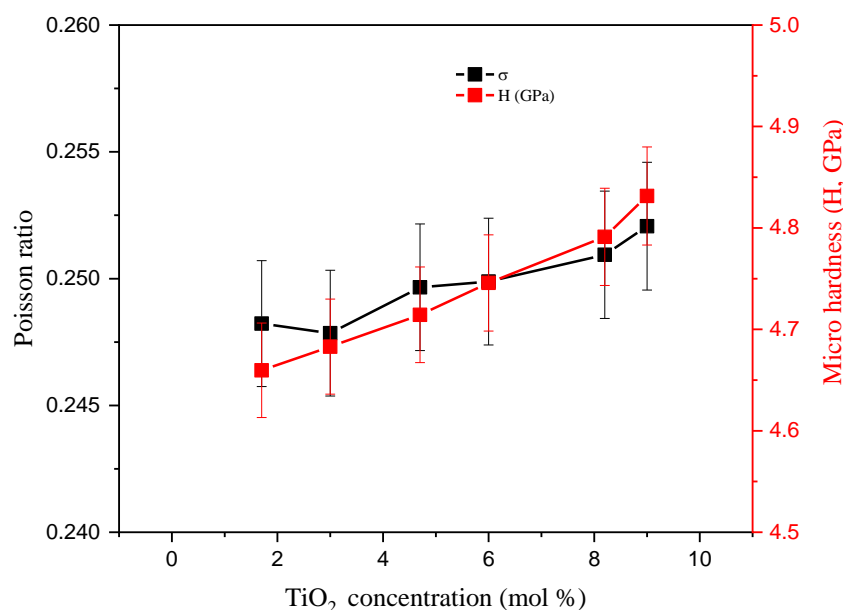


Figure 5. Dependence of the Poisson ratio and microhardness on  $\text{TiO}_2$  concentration.

Declining temperatures were predicted for the investigated glass samples (Table 2). The temperature ( $T_s$ ) slightly increased as the  $\text{TiO}_2$  concentration increased. Samples S1, S2, S3, S4, S5, and S have values of 502.54, 503.09, 502.05, 504.44, 502.05, and 502.59 K, respectively. The slight variation is related to the replacement of  $\text{SiO}_2$  (with a melting point of 1710 °C) with  $\text{TiO}_2$  (melting point 1843 °C). Moreover, the stronger Si-O interatomic bond (field strength ( $F$ ) =  $1.28 \text{ \AA}^{-2}$ ) is substituted with the weaker Ti-O interatomic bond ( $F = 1.54 \text{ \AA}^{-2}$ ). As such, the increase in the thermal expansion coefficient leads to an increase in the  $T_g$  values. Concerning the  $T_g$  values, Takshahi et al. [24], Scannell et al. [25], and Limbach et al. [15] reported a small variation in the  $T_g$  values of  $x\text{Na}_2\text{O}-y\text{TiO}_2-(100-x-y)\text{SiO}_2$  glass system due to the substitution of  $\text{SiO}_2$  by  $\text{TiO}_2$ . However, no such variation was observed by Villegas et al. [26]. These experimental studies are in agreement with our calculations.

Fractal bond conductivity ( $d$ ) was close to 2 for all glass samples. This means that all the samples have a 2D layer structure network, as reported elsewhere [27,28].

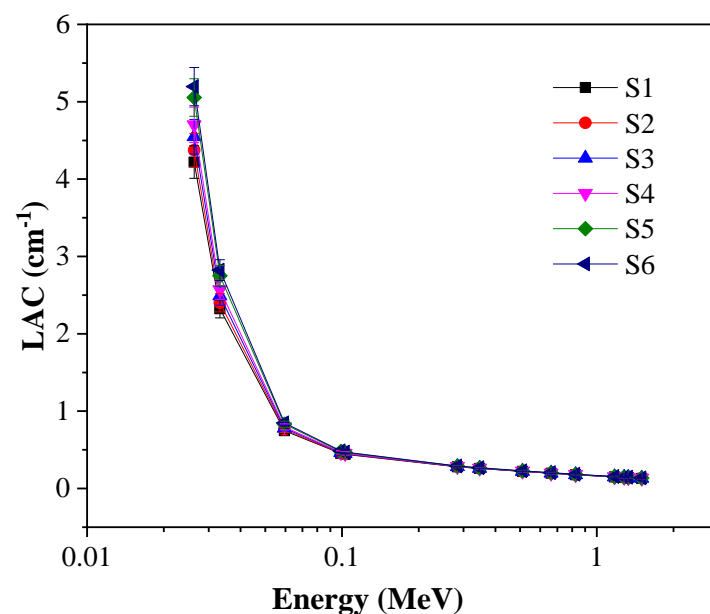
Based on the EM moduli ( $K$  and  $L$ ), both shear velocity ( $v_s$ ) and longitudinal velocity ( $v_l$ ) were predicted and listed in Table 2. Both  $v_l$  and  $v_s$  increase as  $\text{TiO}_2$  increases due to the increase in  $K$  and  $L$ .  $v_l$  varied from 5690.29 to 5756.59 m/s, while  $v_s$  increased from 3293.03 to 3314.36 m/s as  $\text{TiO}_2$  increased from 1.7 to 9 mol%.

**Table 2.** Mechanical properties of the investigated glass samples.

Sample	$V_i$	$v_l$ (m/s)	$v_s$ (m/s)	Softening Temperature ( $T_s$ , °C)	Fractal Bond Conductivity (d)
S1	12.97	5690.29	3293.03	502.54	2.42
S2	12.95	5690.78	3294.95	503.09	2.42
S3	13.00	5713.09	3299.95	502.75	2.40
S4	13.01	5724.26	3305.41	504.44	2.40
S5	12.99	5735.65	3307.32	502.05	2.39
S6	13.00	5756.59	3314.36	502.59	2.38

### 3.2. Shielding Properties

Figure 6 exhibits the LAC against the energy of the incident photons and the concentration of  $\text{TiO}_2$  from 1.7 to 9 mol%. First, let us consider the effect of the energy of incoming photons on LAC values. As shown in Figure 6, at 0.0263 MeV, the highest LAC values are present: photoelectric effect (PE) interactions are predominant, and the PE cross-section is directly proportional to incoming photon energy ( $E^{-3.5}$ ) [29]. As an example, for S1, the LAC values decrease from  $4.2 \text{ cm}^{-1}$  to  $0.13 \text{ cm}^{-1}$  at 0.0263 and 1.5 MeV, respectively. The rapid wane of the LAC values was detected with continuous increase of incoming photon energy. The previous trend in LAC can be demonstrated according to the Compton Scattering (CS) interactions prevalent and its cross-section impacted with the effective atomic number  $Z_{\text{eff}}$  ( $\zeta_{\text{CS}} \propto Z_{\text{eff}}$ ). The LAC values can be disregarded at the high energy range, where the studied glasses provide ineffective shielding. As can be seen at 0.0263 MeV, the LAC values are 4.2 and  $5.19 \text{ cm}^{-1}$  for the glasses with 1.7 mol% (S1) and 9 mol% (S6) of  $\text{TiO}_2$  content, respectively. As opposed to the high photon energy (1.5 MeV), the LAC values are 0.13 and  $0.14 \text{ cm}^{-1}$  for the glasses with  $\text{TiO}_2$  content of 1.7 mol% for S1 and 9 mol%. At constant photon energy values, the LAC values change with the addition of  $\text{TiO}_2$ . MW increased from 60.2 to  $61.77 \text{ g/mol}$  for S1 and S6, respectively, while the density increased from 2.56 to  $2.661 \text{ g/cm}^3$ . Thus, the LAC values rise as  $\text{TiO}_2$  increases from 1.7 to 9 mol%.

**Figure 6.** Change in LAC against incoming gamma-ray energy.

The theoretical mass attenuation coefficient (MAC) was computed using the Phy-X database: the values were compared with the simulated MAC and are listed in Table 3.

**Table 3.** The mass attenuation coefficient of the investigated glass samples using MCNP5 and Phy-X program.

Energy (MeV)	Mass Attenuation Coefficient (cm <sup>2</sup> /g)																	
	S1			S2			S3			S4			S5			S6		
	MCNP-5	Phy-X	Δ (%)	MCNP-5	Phy-X	Δ (%)	MCNP-5	Phy-X	Δ (%)	MCNP-5	Phy-X	Δ (%)	MCNP-5	Phy-X	Δ (%)	MCNP-5	Phy-X	Δ (%)
0.0263	1.648	1.641	0.432	1.705	1.697	0.439	1.753	1.746	0.435	1.805	1.797	0.463	1.916	1.907	0.463	1.953	1.943	0.468
0.0332	0.907	0.907	0.042	0.936	0.935	0.047	0.960	0.960	0.042	0.986	0.986	0.072	1.042	1.042	0.069	1.061	1.060	0.075
0.0595	0.292	0.291	0.105	0.297	0.296	0.113	0.301	0.301	0.110	0.306	0.305	0.128	0.315	0.315	0.132	0.318	0.318	0.132
0.099	0.177	0.177	−0.029	0.178	0.178	−0.027	0.179	0.179	−0.029	0.180	0.180	−0.024	0.182	0.182	−0.026	0.182	0.182	−0.025
0.103	0.172	0.173	−0.037	0.173	0.173	−0.039	0.174	0.174	−0.036	0.175	0.175	−0.032	0.177	0.177	−0.030	0.177	0.177	−0.028
0.284	0.110	0.110	−0.201	0.109	0.110	−0.202	0.109	0.110	−0.203	0.109	0.110	−0.201	0.109	0.110	−0.202	0.109	0.110	−0.203
0.347	0.101	0.101	−0.114	0.101	0.101	−0.115	0.101	0.101	−0.115	0.101	0.101	−0.113	0.101	0.101	−0.115	0.101	0.101	−0.116
0.511	0.086	0.086	−0.105	0.086	0.086	−0.106	0.086	0.086	−0.105	0.086	0.086	−0.105	0.086	0.086	−0.106	0.086	0.086	−0.106
0.662	0.077	0.077	−0.142	0.077	0.077	−0.142	0.077	0.077	−0.141	0.077	0.077	−0.143	0.077	0.077	−0.143	0.076	0.077	−0.143
0.826	0.069	0.069	−0.134	0.069	0.069	−0.134	0.069	0.069	−0.134	0.069	0.069	−0.134	0.069	0.069	−0.134	0.069	0.069	−0.134
1.173	0.058	0.058	−0.363	0.058	0.058	−0.366	0.058	0.058	−0.368	0.058	0.058	−0.371	0.058	0.058	−0.374	0.058	0.058	−0.377
1.28	0.056	0.056	−0.501	0.056	0.056	−0.503	0.056	0.056	−0.505	0.056	0.056	−0.508	0.056	0.056	−0.512	0.056	0.056	−0.513
1.33	0.055	0.055	−0.288	0.055	0.055	−0.290	0.055	0.055	−0.292	0.054	0.055	−0.294	0.054	0.055	−0.221	0.054	0.055	−0.222



The difference ( $\Delta\%$ ) between the theoretical and simulated MAC values is calculated by Equation (11). The difference is lower than 2% for all S glasses.

$$\Delta (\%) = \frac{[(\mu_m)_{mcnp} - (\mu_m)_{xcom}]}{(\mu_m)_{mcnp}} \times 100 \quad (11)$$

The difference ranges over  $-0.288$ – $0.432\%$  for S1,  $-0.290$ – $0.439\%$  for S2,  $-0.292$ – $0.435\%$  for S3,  $-0.294$ – $0.463\%$  for S4,  $-0.221$ – $0.463$  and  $-0.222$ – $0.468\%$  for S6. Figure 7 illustrates the inconsistent comparison of the theoretically computed data with the simulated coefficients. From this, it is plain that gaps are not observed between the Phy-X and MCNP5 data. In general, the computed results from MAC via Phy-X are slightly lower than the simulated results using MCNP5. This may have been caused by the fact that the Phy-X code does not include the effects of the atomic wave mechanism on molecular bonding, which may lead to a decrease in MAC in such compounds. The smallness of the relative deviations can be ascribed to the precision of the code's physics models [30,31].

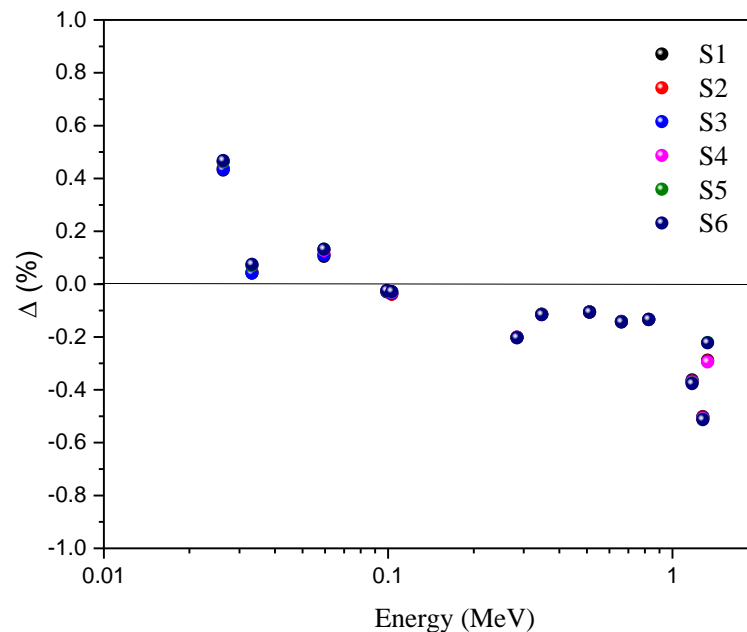


**Figure 7.** Ratios of MAC values computed by Phy-X against those simulated with the MCNP code.

Unlike LAC, the simulated HVL values increase as the incoming gamma photon energy increase (Figure 8). These values demonstrate the ability of the investigated glasses to reduce the incoming gamma photon energy by half. The simulated HVL reached maximum values of 5.2 and 5.08 cm at high gamma energy (1.5 MeV) for S1 and S6. This means that the glasses with low simulated HVL value can be applied as radiation shielding. S6 glasses have low simulated HVL values at the applied range of incoming gamma photon energy (0.0263–1.5 MeV).

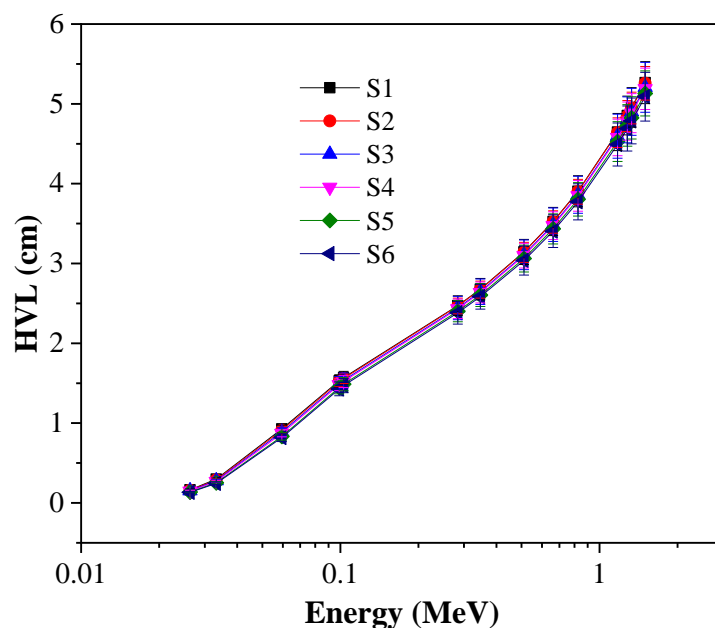


Figure 8. HVL of glasses as a function of energy.

Figure 9 depicts how  $\text{TiO}_2$  content influenced the HVL values. The computer program Phy-x/PD was used to compute the theoretical HVL values at varying incoming photon energies (0.015–15 MeV). As can be noted, the HVL values decreased as  $\text{TiO}_2$  content increased from 1.7 to 9 mol% at a stationary photon energy. At all selected photon energies, the lowest HVL values are achieved by S6, while the highest are observed for S1.

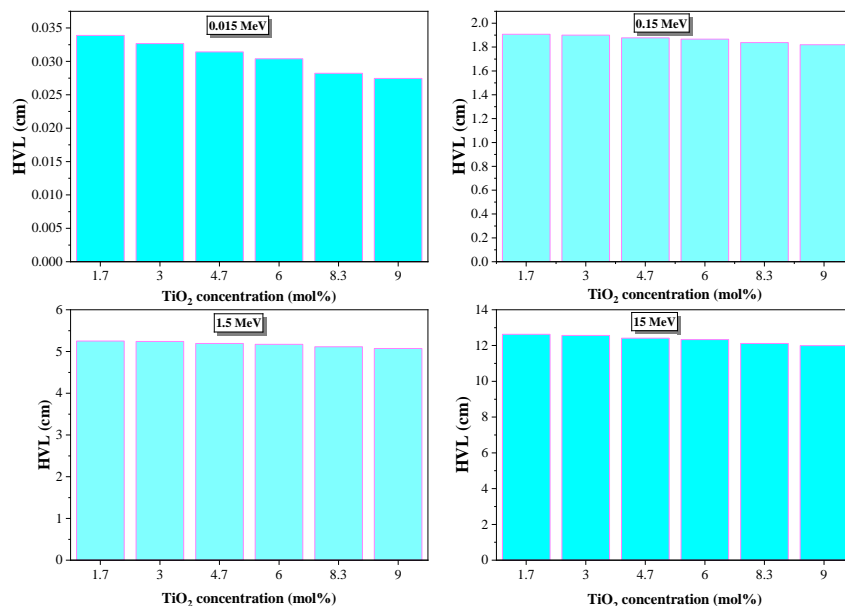


Figure 9. Changes in HVL in the glasses at stationary gamma photon energy (0.015, 0.15, 1.5, and 15 MeV).

Further, the effective atomic number ( $Z_{\text{eff}}$ ), the equivalent atomic number ( $Z_{\text{eq}}$ ), the exposure build-up factor (EBF), and the energy absorption build-up factor (EABF) were computed through the Phy-x/PD. The data are presented in Figures 10–13 and are discussed in the following.

First, the effective atomic number ( $Z_{\text{eff}}$ ) values have been observed so that we can study the ability of the glasses to be used as shielding against gamma radiation. Figures 10 and 11

show the  $Z_{\text{eff}}$  profile for the tested glasses. In Figure 10, the  $Z_{\text{eff}}$  values are affected by the energy of the incoming photons. In the selected energy range, three main interactions are detected. The first interaction is PE, which possesses a photon energy range of 0.015–0.1 MeV; this changed with  $Z^4$  and the maximum  $Z_{\text{eff}}$  values. Clearly, the  $Z_{\text{eff}}$  values drop quickly as photon energy increases. When photon energy increases above 0.1 MeV, the CS interaction is predominant:  $Z_{\text{eff}}$  gradually decreases. At photon energy levels greater than several MeV,  $Z_{\text{eff}}$  starts to increase. This change is attributed to the pair production (PP) interaction, which is predominant at high gamma-ray energy intervals. The PP interaction cross-section directly changes with  $Z^2$  [32].

Figures 10 and 11 show that the  $Z_{\text{eff}}$  values decline when  $\text{TiO}_2$  increases from 1.7 to 9 mol%. Thus, the insertion of  $\text{TiO}_2$  enhances shielding effectiveness significantly. S6 is the most promising sample for radiation protection compared to the others.

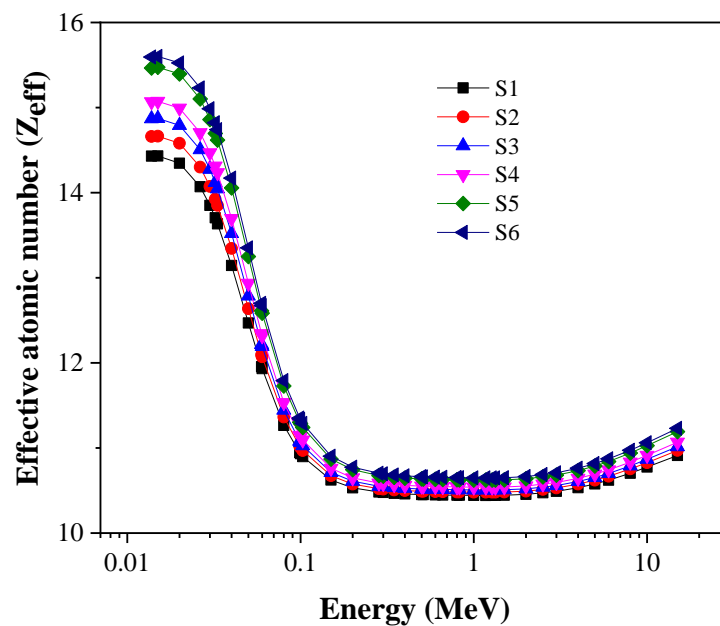


Figure 10. Change in  $Z_{\text{eff}}$  as a function of gamma-photon energy.

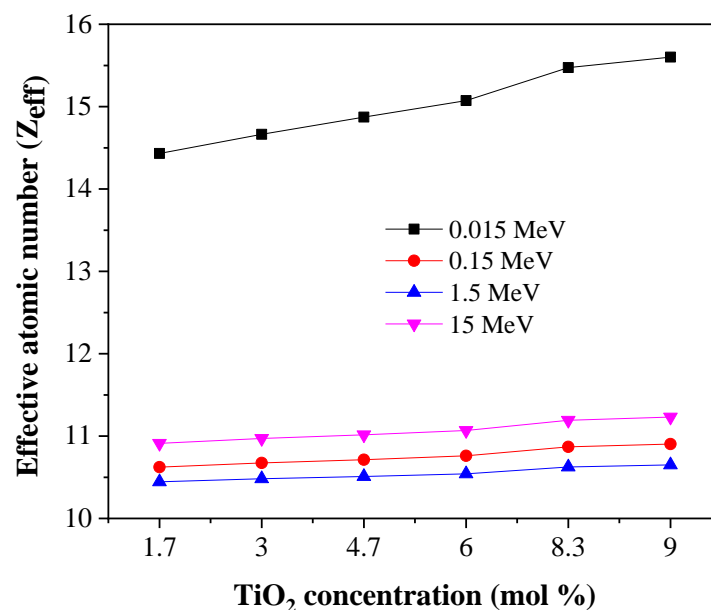


Figure 11. Change in  $Z_{\text{eff}}$  at a fix four photon energies.

The second factor is the  $Z_{eq}$ , which is calculated based on the MACCS values and presented in Figure 12. The values of  $Z_{eq}$  increased as the energy increased from 0.015 to 1 MeV. The equivalent atomic number reaches the highest values in the CS region, the intermediate photon energy range. At the same time, the minimum values of  $Z_{eq}$  are achieved in the high-energy region, where the PP interactions occur. The maximum values of  $Z_{eq}$  increase from 12.78 to 13.51 for S1 and S6, respectively, while the minimum values increase from 11.56 to 12.02 for S1 and S6, respectively.

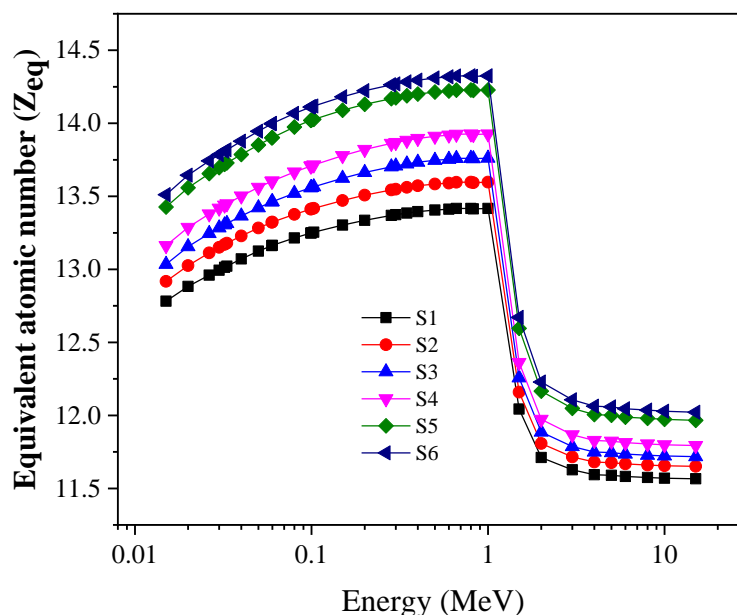


Figure 12. Change in equivalent atomic number ( $Z_{eq}$ ) against incoming photon energy.

EBF and EABF are two factors used to determine the total flux of gamma radiation. The variation of both parameters with the incoming energy for S1 and S6 is presented in Figure 13. Moreover, Table 4 illustrates the G-P fitting factors of the EBF and EABF values for S6, which is optimized at gamma energies ranging from 0.015 to 15 MeV.

Table 4. G-P fitting parameters for S6 at various gamma photon energies.

E (MeV)	$Z_{eq}$	EBF					EABF				
		a	b	c	d	$X_k$	a	b	c	d	$X_k$
0.015	13.51	0.24	1.03	0.37	-0.16	13.67	0.21	1.03	0.39	-0.12	12.58
0.02	13.65	0.19	1.06	0.41	-0.11	16.31	0.2	1.06	0.4	-0.11	16.47
0.03	13.79	0.21	1.19	0.4	-0.11	14.22	0.21	1.19	0.4	-0.12	14.33
0.04	13.88	0.19	1.4	0.47	-0.10	14.38	0.19	1.41	0.46	-0.10	14.64
0.05	13.95	0.13	1.65	0.58	-0.07	15.18	0.12	1.69	0.6	-0.06	16.73
0.06	14	0.09	1.89	0.7	-0.05	15.29	0.14	2.18	0.6	-0.08	13.56
0.08	14.07	0.06	2.39	0.83	-0.05	14.54	0.07	3.04	0.81	-0.05	13.96
0.1	14.11	0.01	2.6	1.01	-0.03	13.7	0.01	3.68	1.02	-0.03	13.76
0.15	14.18	-0.04	2.71	1.26	-0.01	10.63	-0.06	4.03	1.33	0.01	15.07
0.2	14.22	-0.06	2.66	1.36	-0.01	8.02	-0.08	3.69	1.48	0.02	14.78
0.3	14.27	-0.08	2.47	1.46	0.01	17.52	-0.10	3.12	1.57	0.03	14.37
0.4	14.3	-0.08	2.35	1.46	0.02	16.23	-0.10	2.79	1.56	0.03	14.77
0.5	14.31	-0.08	2.24	1.45	0.02	16.3	-0.09	2.58	1.53	0.03	15.01
0.6	14.32	-0.08	2.17	1.42	0.02	17.94	-0.09	2.44	1.49	0.03	14.99
0.8	14.32	-0.07	2.05	1.38	0.02	15.4	-0.08	2.24	1.42	0.03	15.12
1	14.33	-0.06	1.97	1.32	0.02	16.21	-0.07	2.12	1.36	0.02	14.99
1.5	12.67	-0.05	1.86	1.23	0.02	15.53	-0.05	1.94	1.25	0.02	14.65
2	12.23	-0.03	1.79	1.15	0.01	15.92	-0.04	1.83	1.16	0.01	14.53
3	12.11	-0.01	1.67	1.06	0	15.86	-0.01	1.7	1.06	0	14.34

Table 4. Cont.

E (MeV)	$Z_{eq}$	EBF					EABF				
		a	b	c	d	$X_k$	a	b	c	d	$X_k$
4	12.06	0.01	1.6	1	−0.01	12.97	0.01	1.61	0.99	−0.01	14.35
5	12.06	0.02	1.54	0.94	−0.02	10.21	0.03	1.55	0.92	−0.03	13.09
6	12.05	0.02	1.48	0.93	−0.02	12.02	0.02	1.47	0.93	−0.03	15.4
8	12.04	0.03	1.4	0.9	−0.03	13.85	0.03	1.38	0.91	−0.02	12.04
10	12.03	0.04	1.34	0.89	−0.03	13.09	0.03	1.31	0.92	−0.03	14.56
15	12.02	0.06	1.25	0.85	−0.05	14.25	0.06	1.23	0.84	−0.05	14.16

Figure 13 displays the change in the EBF and EABF values as incoming photon energy increases up to 15 MeV. The minimum EBF and EABF are realized in the low-energy region. This is associated with the photoelectric process, which means all incident gamma photons will pass through the glass. Otherwise, the values of EBF and EABF increase as the incoming photon energy increases in the middle photon energy range. This is due to the track of multiplied scattering photons from the Compton process. This clarifies the number of incident gamma photons interacting and penetrating the glass material: the remaining photons are scattered, inducing more interactions. Therefore, multiple photons accumulate inside the glass material. Finally, in the high energy range, the EBF and EABF values reach their maximum values, which is associated with the PP process [33,34].

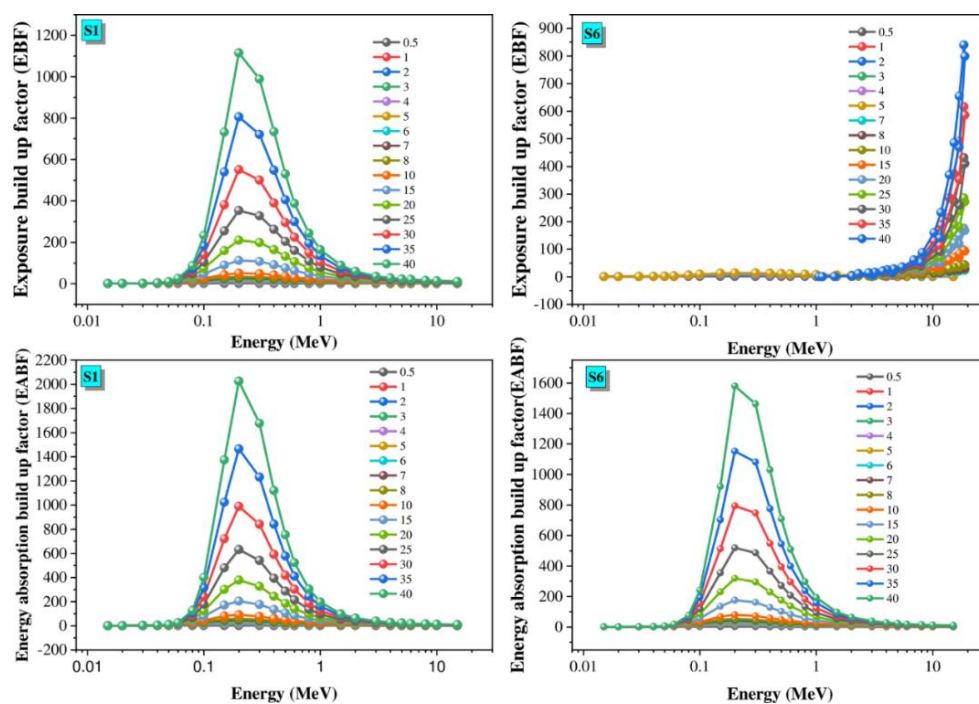


Figure 13. Dependence of EBF and EABF on the radiation energy.

Moreover, the buildup factors were affected by penetration depth (PD, mfp), which varied from 0.5 to 40 mfp at the four selected photon energies. The buildup factors depend on the composition of the samples (Figures 14 and 15). The correlation between EBF, EABF, and PD values is clearly shown in Figures 14 and 15. The glasses with the lowest PD value have low EBF and EABF values because the incident gamma photons spend only a short time inside the material. At the same time, the highest values are due to the long period that photons spend within the glass. Furthermore,  $TiO_2$  in the glasses leads to an increase in the buildup factors.

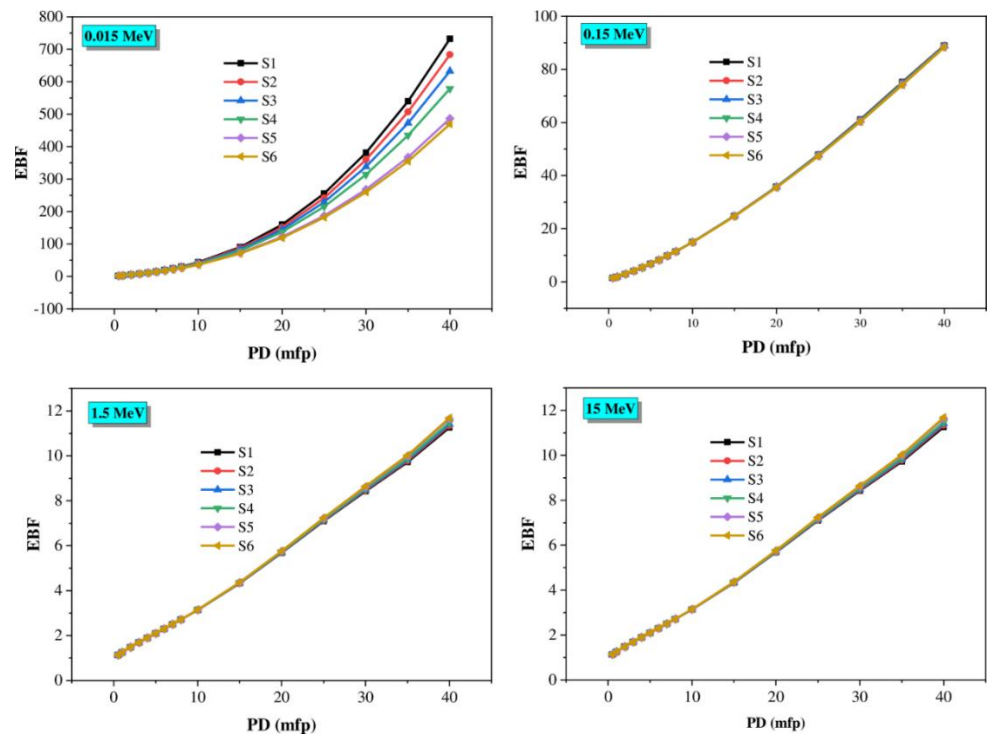


Figure 14. EBF changes against the penetration depth of the glasses at various gamma photon energies (0.015, 0.15, 1.5, and 15 MeV).

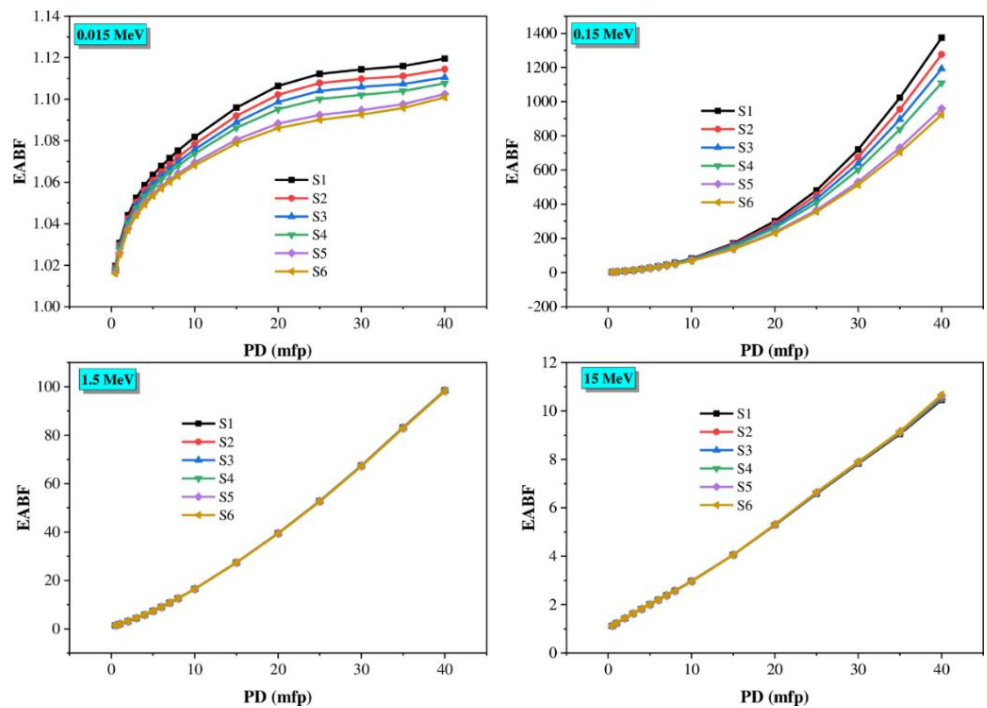


Figure 15. EABF changes against the penetration depth of the glasses at various gamma photon energies (0.015, 0.15, 1.5, and 15 MeV).

#### 4. Conclusions

In this study, we have considered the effect of replacing SiO<sub>2</sub> with TiO<sub>2</sub> on the mechanical and radiation shielding properties of a quaternary glass system consisting of Na<sub>2</sub>O, CaO, SiO<sub>2</sub>, and TiO<sub>2</sub>. The partial replacement of SiO<sub>2</sub> showed enhanced elastic moduli, and radiation shielding of the glass system. The Young module increased from 69.30 to

73.20 GPa as TiO<sub>2</sub> content increased from 1.7 to 9 mol%. The bulk, shear, and longitudinal moduli followed the same trend. The microhardness increased from 4.66 to 4.83 GPa as the SiO<sub>2</sub> substitution ratio increased. The radiation shielding properties were evaluated using MCNP-5 and the Phy-X/PSD program between 0.015 and 15 MeV, which covers the entire experimental energy range. Both Phy-X/PSD and MCNP-5 results are in good agreement. The highest LAC value was detected at 0.015 MeV: it increased from 4.22 to 5.20 cm<sup>-1</sup> as the TiO<sub>2</sub> concentration increased from 1.7 to 9 mol%. The EBF and EABF calculations showed that the replacement of SiO<sub>2</sub> with TiO<sub>2</sub> reduces photon accumulation. The advantages of the present glass samples means they offer good low-cost shielding for the low- and mid-energy regions.

**Author Contributions:** Conceptualization, M.Y.H., M.I.S. and K.A.M.; methodology, A.H.A.; software, K.A.M.; validation, B.A., A.H.A. and M.I.S.; formal analysis, M.Y.H.; investigation, K.A.M.; resources, B.A.; data curation, H.M.A.; writing—original draft preparation, M.Y.H., H.M.A. and K.A.M.; writing—review and editing, M.Y.H., M.I.S. and K.A.M.; visualization, M.I.S.; supervision, M.I.S.; project administration, A.H.A.; funding acquisition, B.A. All authors have read and agreed to the published version of the manuscript.

**Funding:** This research was funded by the Deanship of Scientific Research at Princess Nourah bint Abdulrahman University through the Fast-Track Research Funding Program.

**Institutional Review Board Statement:** Not applicable.

**Informed Consent Statement:** Not applicable.

**Data Availability Statement:** The data presented in this study are available on request from the corresponding author.

**Conflicts of Interest:** The authors declare no conflict of interest.

## References

1. Nagaraja, N.; Manjunatha, H.; Seenappa, L.; Sathish, K.; Sridhar, K.; Ramalingam, H. Gamma, X-ray and neutron shielding properties of boron polymers. *Indian J. Pure Appl. Phys.* **2020**, *58*, 271–276.
2. Singh, K.; Singh, S.; Dhaliwal, A.S.; Singh, G. Gamma radiation shielding analysis of lead-flyash concretes. *Appl. Radiat. Isot.* **2015**, *95*, 174–179. [[CrossRef](#)]
3. Composites, P.T.; Wu, Y.; Cao, Y.; Wu, Y.; Li, D. Mechanical Properties and Gamma-Ray Shielding Performance of 3D-Printed. *Materials* **2020**, *13*, 4475. [[CrossRef](#)]
4. Mahmoud, K.A.; Tashlykov, O.L.; El Wakil, A.F.; El Aassy, I.E. Aggregates grain size and press rate dependence of the shielding parameters for some concretes. *Prog. Nucl. Energy* **2020**, *118*, 103092. [[CrossRef](#)]
5. Rammah, Y.S.; Askin, A.; Abouhaswa, A.S.; El-Agawany, F.I.; Sayyed, M.I. Synthesis, physical, structural and shielding properties of newly developed B<sub>2</sub>O<sub>3</sub>–ZnO–PbO–Fe<sub>2</sub>O<sub>3</sub> glasses using Geant4 code and WinXCOM program. *Appl. Phys. A Mater. Sci. Process.* **2019**, *125*. [[CrossRef](#)]
6. Kurudirek, M. Radiation shielding and effective atomic number studies in different types of shielding concretes, lead base and non-lead base glass systems for total electron interaction: A comparative study. *Nucl. Eng. Des.* **2014**, *280*, 440–448. [[CrossRef](#)]
7. Kaundal, R.S. Comparative study of radiation shielding parameters for binary oxide glasses. *Orient. J. Chem.* **2017**, *33*, 2324–2328. [[CrossRef](#)]
8. Demirbay, T.; Çağlar, M.; Karabul, Y.; Kılıç, M.; İçelli, O.; Güven Özdemir, Z. Availability of water glass/Bi<sub>2</sub>O<sub>3</sub> composites in dielectric and gamma-ray screening applications. *Radiat. Eff. Defects Solids* **2019**, *174*, 419–434. [[CrossRef](#)]
9. Muthamma, M.V.; Gudennavar, B.S.; Gudennavar, S.B. Attenuation parameters of polyvinyl alcohol-tungsten oxide composites at the photon energies 5.895, 6.490, 59.54 and 662 keV. *Polish J. Med. Phys. Eng.* **2020**, *26*, 77–85. [[CrossRef](#)]
10. Lakshminarayana, G.; Elmahroug, Y.; Kumar, A.; Tekin, H.O.; Rekik, N.; Dong, M.; Lee, D.E.; Yoon, J.; Park, T. Detailed inspection of  $\gamma$ -ray, fast and thermal neutrons shielding competence of calcium oxide or strontium oxide comprising bismuth borate glasses. *Materials* **2021**, *14*, 2265. [[CrossRef](#)]
11. Kaewjaeng, S.; Kaewkhao, J.; Limsuwan, P.; Maghanemi, U. Effect of BaO on optical, physical and radiation shielding properties of SiO<sub>2</sub>–B<sub>2</sub>O<sub>3</sub>–Al<sub>2</sub>O<sub>3</sub>–CaO–Na<sub>2</sub>O glasses system. *Procedia Eng.* **2012**, *32*, 1080–1086. [[CrossRef](#)]
12. Ruengsri, S. Radiation shielding properties comparison of Pb-based silicate, borate, and phosphate glass matrices. *Sci. Technol. Nucl. Install.* **2014**, *2014*. [[CrossRef](#)]
13. Kharita, M.H.; Jabra, R.; Yousef, S.; Samaan, T. Shielding properties of lead and barium phosphate glasses. *Radiat. Phys. Chem.* **2012**, *81*, 1568–1571. [[CrossRef](#)]

14. Tashlykov, O.L.; Vlasova, S.G.; Kovyazina, I.S.; Mahmoud, K.A. Repercussions of yttrium oxides on radiation shielding capacity of sodium-silicate glass system: Experimental and Monte Carlo simulation study. *Eur. Phys. J. Plus* **2021**, *136*, 428. [[CrossRef](#)]
15. Limbach, R.; Karlsson, S.; Scannell, G.; Mathew, R.; Edén, M.; Wondraczek, L. The effect of TiO<sub>2</sub> on the structure of Na<sub>2</sub>O-CaO-SiO<sub>2</sub> glasses and its implications for thermal and mechanical properties. *J. Non Cryst. Solids* **2017**, *471*, 6–18. [[CrossRef](#)]
16. Makishima, A.; Mackenzie, J.D. Direct calculation of Young's modulus of glass. *J. Non Cryst. Solids* **1973**, *12*, 35–45. [[CrossRef](#)]
17. Makishima, A.; Mackenzie, J.D. Calculation of bulk modulus, shear modulus and Poisson's ratio of glass. *J. Non. Cryst. Solids* **1975**, *17*, 147–157. [[CrossRef](#)]
18. El-Adawy, A.; El-KheshKhany, N. Effect of rare earth (Pr<sub>2</sub>O<sub>3</sub>, Nd<sub>2</sub>O<sub>3</sub>, Sm<sub>2</sub>O<sub>3</sub>, Eu<sub>2</sub>O<sub>3</sub>, Gd<sub>2</sub>O<sub>3</sub> and Er<sub>2</sub>O<sub>3</sub>) on the acoustic properties of glass belonging to bismuth-borate system. *Solid State Commun.* **2006**, *139*, 108–113. [[CrossRef](#)]
19. General, M.A.; Carlo, M. *LA-UR-03-1987 X-5 Monte Carlo Team*; Los Alamos National Laboratory: Los Alamos, NM, USA, 2003; Volume 836.
20. Erdem, Ş.; Özgür, F.; Al, B.; Sayyed, M.I.; Kurudirek, M. Phy-X/PSD: Development of a user friendly online software for calculation of parameters relevant to radiation shielding and dosimetry. *Radiat. Phys. Chem.* **2020**, *166*. [[CrossRef](#)]
21. Mahmoud, K.A.; Tashlykov, O.L.; Mhareb, M.H.A.; Almuqrin, A.H.; Alajerami, M.; Sayyed, M.I. A new heavy-mineral doped clay brick for gamma-ray protection purposes. *Appl. Radiat. Isot.* **2021**, *173*, 109720. [[CrossRef](#)] [[PubMed](#)]
22. Kumar, A.; Jain, A.; Sayyed, M.I.; Laariedh, F.; Mahmoud, K.A.; Nebhen, J.; Khandaker, M.U.; Faruque, M.R.I. Tailoring bismuth borate glasses by incorporating PbO/GeO<sub>2</sub> for protection against nuclear radiation. *Sci. Rep.* **2021**, *11*, 1–14. [[CrossRef](#)]
23. Inaba, S.; Fujino, S.; Morinaga, K. Young's modulus and compositional parameters of oxide glasses. *J. Am. Ceram. Soc.* **1999**, *82*, 3501–3507. [[CrossRef](#)]
24. Takahashi, K.; Mochida, N.; Yoshida, Y. Properties and structure of silicate glasses containing tetravalent cations. *J. Ceram Soc. Jpn.* **1977**, *85*, 330–340.
25. Scannell, G.; Huang, L.; Rouxel, T. Elastic properties and indentation cracking behavior of Na<sub>2</sub>O-TiO<sub>2</sub>-SiO<sub>2</sub> glasses. *J. Non-Cryst. Solids* **2015**, *429*, 129–142. [[CrossRef](#)]
26. Villegas, M.A.; Depablos, A.; Fernandeznavarro, J.M. Properties of CaO-TiO<sub>2</sub>-SiO<sub>2</sub> glasses. *Glass Technol.* **1994**, *35*, 276–280.
27. Saunders, G.A.; Brennan, T.; Acet, M.; Cankurtaran, M.; Senin, H.B.; Sidek, H.A.A.; Federico, M. Elastic and non-linear acoustic properties and thermal expansion of cerium metaphosphate glasses. *J. Non Cryst. Solids* **2001**, *282*, 291–305. [[CrossRef](#)]
28. Alazoumi, S.H.; Sidek, H.A.A.; Halimah, M.K.; Matori, K.A.; Zaid, M.H.M.; Abdulbaset, A.A. Synthesis and elastic properties of ternary ZnO-PbO-TeO<sub>2</sub> glasses. *Chalcogenide Lett.* **2017**, *14*, 303–320.
29. Hehn, G. Principles of Radiation Shielding. *Nucl. Technol.* **1986**, *74*, 104–105. [[CrossRef](#)]
30. Medhat, M.E.; Wang, Y. Geant4 code for simulation attenuation of gamma rays through scintillation detectors. *Ann. Nucl. Energy* **2013**, *62*, 316–320. [[CrossRef](#)]
31. Singh, V.P.; Medhat, M.E.; Shirmardi, S.P. Comparative studies on shielding properties of some steel alloys using Geant4, MCNP, WinXCOM and experimental results. *Radiat. Phys. Chem.* **2015**, *106*, 255–260. [[CrossRef](#)]
32. Singh, V.P.; Badiger, N.M.; Kaewkhao, J. Radiation shielding competence of silicate and borate heavy metal oxide glasses: Comparative study. *J. Non Cryst. Solids* **2014**, *404*, 167–173. [[CrossRef](#)]
33. Mahmoud, K.A.; El-Agwany, F.I.; Rammah, Y.S.; Tashlykov, O.L. Gamma ray shielding capacity and build up factors of CdO doped lithium borate glasses: Theoretical and simulation study. *J. Non Cryst. Solids* **2020**, *541*, 120110. [[CrossRef](#)]
34. Rammah, Y.S.; Mahmoud, K.A.; Sayyed, M.I.; El-Agawany, F.I.; El-Mallawany, R. Novel vanadyl lead-phosphate glasses: P<sub>2</sub>O<sub>5</sub>-PbO-ZnO[~~sbnd~~]Na<sub>2</sub>O-V<sub>2</sub>O<sub>5</sub>: Synthesis, optical, physical and gamma photon attenuation properties. *J. Non Cryst. Solids* **2020**, *534*, 119944. [[CrossRef](#)]